



1 **A novel formation mechanism of NH<sub>2</sub>SO<sub>3</sub>H and its enhancing effect**  
2 **on methanesulfonic acid-methylamine aerosol particle formation in**  
3 **agriculture-developed and coastal industrial areas**

4 **Hui Wang<sup>a,‡</sup>, Shuqin Wei<sup>a,‡</sup>, Jihuan Yang<sup>a</sup>, Yanlong Yang<sup>a</sup>, Rongrong Li<sup>a</sup>, Rui Wang<sup>a</sup>,**  
5 **Chongqin Zhu<sup>b,\*</sup>, Tianlei Zhang<sup>a,\*</sup>, Changming Zhang<sup>c</sup>**

6 <sup>a</sup> Shaanxi Key Laboratory of Catalysis, School of Chemical & Environment Science, Shaanxi  
7 University of Technology, Hanzhong, Shaanxi 723001, P. R. China

8 <sup>b</sup> College of Chemistry, Key Laboratory of Theoretical & Computational Photochemistry of  
9 Ministry of Education, Beijing Normal University, Beijing 100190, China.

10 <sup>c</sup> School of Mechanical Engineering, Shaanxi University of Technology, Hanzhong, Shaanxi 723001,  
11 P. R. China

12 **Abstract**

13 Sulfamic acid (SFA) significantly impacts atmospheric pollution and poses potential risks to human  
14 health. Although traditional source of SFA and its role on sulfuric acid-dimethylamine new particle  
15 formation (NPF) has received increasing attention, the formation mechanism of SFA from HNSO<sub>2</sub>  
16 hydrolysis with CH<sub>3</sub>SO<sub>3</sub>H and its enhancing effect on methanesulfonic acid-methylamine APF has  
17 not been studied, which will limit the understanding for the source and loss of SFA in agriculture-  
18 developed and coastal industrial areas. Here, the gaseous and interfacial formation of SFA from  
19 HNSO<sub>2</sub> hydrolysis with CH<sub>3</sub>SO<sub>3</sub>H was investigated using quantum chemical calculations and  
20 BOMD simulations. Furthermore, the role of SFA in CH<sub>3</sub>SO<sub>3</sub>H-CH<sub>3</sub>NH<sub>2</sub> system was assessed using  
21 the Atmospheric Cluster Dynamics Code kinetic model. Our simulation results indicate that the  
22 gaseous SFA formation from the hydrolysis of HNSO<sub>2</sub> with CH<sub>3</sub>SO<sub>3</sub>H can be competitive with that  
23 catalyzed by H<sub>2</sub>O within an altitude of 5-15 km. At the air-water interface, two types of reactions,  
24 the ions forming mechanism and the proton exchange mechanism to form NH<sub>2</sub>SO<sub>3</sub><sup>-</sup>⋯H<sub>3</sub>O<sup>+</sup> ion pair  
25 were observed on the timescale of picosecond. Considering the overall environment of sulfuric acid  
26 emission reduction, the present findings suggest that SFA may play a significant role in NPF and  
27 the growth of aerosol particle as *i*) SFA can directly participate in the formation of CH<sub>3</sub>SO<sub>3</sub>H-  
28 CH<sub>3</sub>NH<sub>2</sub>-based cluster and enhance the rate of NPF from these clusters by approximately 10<sup>3</sup> times  
29 at 278.15 K; and *ii*) the NH<sub>2</sub>SO<sub>3</sub><sup>-</sup> species at the air-water interface can attract gaseous molecules to  
30 the aqueous surface, and thus promote particle growth.

\* Corresponding authors, Tel: +86-0916-2641083, Fax: +86-0916-2641083.  
E-mail: [cqzhu@bnu.edu.cn](mailto:cqzhu@bnu.edu.cn) (C. Q. Zhu), [ztianlei88@163.com](mailto:ztianlei88@163.com) (T. L. Zhang).

<sup>‡</sup> These authors contributed equally to this work.



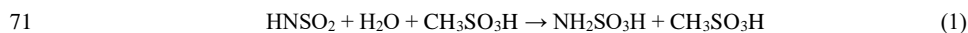
## 31 **1 Introduction**

32 As a well-studied nitrogen derivative of sulfuric acid (Rennebaum et al., 2024), sulfamic acid  
33 ( $\text{NH}_2\text{SO}_3\text{H}$ ) was not only recognized as a potent aerosol and cloud nucleating agent (Xue et al.,  
34 2024; Zhang et al., 2023; Pszona et al., 2015; Li et al., 2018), but also can harm human health  
35 through atmospheric deposition into water bodies (Van Stempvoort et al., 2019). In agriculture-  
36 developed and industrial areas with high ammonia ( $\text{NH}_3$ ) concentrations, such as the Yangtze River  
37 Delta in China (Yu et al., 2020), Indo-Gangetic Plains (Kuttippurath et al., 2020), Pakistan,  
38 Bangladesh (Warner et al., 2016), and the southern Italy (Tang et al., 2021), the atmospheric  
39 concentration of  $\text{NH}_2\text{SO}_3\text{H}$  was expected to reach up to  $10^8$  molecules· $\text{cm}^{-3}$  (Li et al., 2018), and  
40 thus lead to it becoming a significant air pollutant. So, the sources of  $\text{NH}_2\text{SO}_3\text{H}$  in the atmosphere  
41 have been well investigated (Lovejoy and Hanson, 1996; Pszona et al., 2015; Li et al., 2018; Larson  
42 and Tao, 2001; Manonmani et al., 2020; Zhang et al., 2022). The traditional source of  $\text{NH}_2\text{SO}_3\text{H}$   
43 was mainly taken from the ammonolysis of  $\text{SO}_3$  (Lovejoy and Hanson, 1996; Larson and Tao, 2001;  
44 Li et al., 2018). Experimentally, the rate coefficient for the ammonolysis of  $\text{SO}_3$  was detected to be  
45  $2.0 \times 10^{-11}$   $\text{cm}^3\cdot\text{molecules}^{-1}\cdot\text{s}^{-1}$  at 295 K (Lovejoy and Hanson, 1996), which was close to the value  
46 for the hydrolysis of  $\text{SO}_3$  assisted by water molecule ( $10^{-11}$ - $10^{-10}$   $\text{cm}^3$   $\text{molecule}^{-1}$   $\text{s}^{-1}$ ) (Kim et al.,  
47 1998; Hirota et al., 1996; Shi et al., 1994). Theoretically, the ammonolysis of  $\text{SO}_3$  to produce  
48  $\text{NH}_2\text{SO}_3\text{H}$  can be catalyzed by  $\text{NH}_3$ . In arid and heavily polluted regions with high  $\text{NH}_3$   
49 concentrations, the effective rate coefficient for the ammonolysis of  $\text{SO}_3$  can be sufficiently rapid,  
50 making it competitive with the conventional loss pathway of  $\text{SO}_3$  with water (Li et al., 2018).

51 In addition to the ammonolysis of  $\text{SO}_3$ , new sources of  $\text{NH}_2\text{SO}_3\text{H}$  formation have received  
52 increasing attention (Zhang et al., 2022; Manonmani et al., 2020, Li et al., 2018, Xue et al., 2024).  
53 The existence of  $\text{HNSO}_2$  was proposed in the reaction between  $\text{SO}_3$  and  $\text{NH}_3$ , and was regarded as  
54 the most stable for nine different isomers of  $\text{HNSO}_2$ ,  $\text{HONSO}$ ,  $\text{HOSNO}$ ,  $\text{HOS(O)N}$ ,  $\text{HSNO}_2$ ,  
55  $\text{HSONO}$ ,  $\text{HON(O)S}$ ,  $\text{HOOSN}$ , and  $\text{HOONS}$  (Deng et al., 2016). Owing to its similarity with  $\text{SO}_3$   
56 and the potential role of  $\text{SO}_3$  in the atmosphere, the hydrolysis of  $\text{HNSO}_2$  to produce  $\text{NH}_2\text{SO}_3\text{H}$   
57 formation has been focused by several groups (Zhang et al., 2022; Manonmani et al., 2020). As the  
58 direct hydrolysis of  $\text{HNSO}_2$  with a high energy barrier takes place hardly in the gas phase (Zhang  
59 et al., 2022; Manonmani et al., 2020), the addition of a second water molecule (Manonmani et al.,



60 2020), formic acid and sulfuric acid ( $\text{H}_2\text{SO}_4$ , SA) (Zhang et al., 2022) have been proved to promote  
61 the product of  $\text{NH}_2\text{SO}_3\text{H}$  through the hydrolysis of  $\text{HNSO}_2$ . However, to the best of our knowledge,  
62 the gaseous hydrolysis of  $\text{HNSO}_2$  with  $\text{CH}_3\text{SO}_3\text{H}$  has not yet been investigated. It was noted that,  
63 with the global reduction in the concentration of  $\text{H}_2\text{SO}_4$  resulting from  $\text{SO}_2$  emission restrictions,  
64 the contribution of  $\text{CH}_3\text{SO}_3\text{H}$  to aerosol nucleation has received the widespread attention of  
65 scientists. As a major inorganic acidic air pollutant (Chen et al., 2020), the concentration of  
66  $\text{CH}_3\text{SO}_3\text{H}$  in the atmosphere was noted to be notably high across various regions, spanning from  
67 coastal to continental, with levels found to be between 10% and 250% of those measured for SA  
68 (Shen et al., 2019; Dawson et al., 2012; Bork et al., 2014; Shen et al., 2020; Berresheim et al., 2002;  
69 Hu et al., 2023). Thus, understanding the hydrolysis of  $\text{HNSO}_2$  with  $\text{CH}_3\text{SO}_3\text{H}$  in the gas phase was  
70 necessary for exploring its impact on aerosols and human health.



72 As a supplement to gas-phase reactions, interfacial reactions at the air-water interface not only  
73 can accelerate the rates of atmospheric reactions but also may introduce new mechanisms (Freeling  
74 et al., 2020; Zhong et al., 2019). For instance, the Criegee intermediates reacting with  $\text{CH}_3\text{SO}_3\text{H}$  at  
75 the air-water interface can form the ion pair of  $\text{CH}_3\text{C}(\text{H})(\text{OOH})(\text{SO}_3\text{CH}_3)$  anhydride and  $\text{H}_3\text{O}^+$  (Ma  
76 et al., 2020), which differs from the corresponding gaseous reaction where the  $\text{CH}_3\text{SO}_3\text{H}$  molecule  
77 acts solely as a reactant reacting with Criegee intermediates directly. As far as we know,  $\text{HNSO}_2$   
78 exhibit a significant interfacial preference, as the fact that the total duration time of  $\text{HNSO}_2$  at the  
79 interface approximately accounts for 49.1% of the 150 ns simulation time (Fig. S1). However, the  
80 hydrolysis of  $\text{HNSO}_2$  with  $\text{CH}_3\text{SO}_3\text{H}$  has not been studied at the air-water interface, which will  
81 confine the understanding for the source of  $\text{NH}_2\text{SO}_3\text{H}$  in regions with significant pollution and high  
82 levels of  $\text{CH}_3\text{SO}_3\text{H}$ .

83 From a structural point of view, two functional groups of  $-\text{NH}_2$  and  $-\text{SO}_3\text{H}$  in the  $\text{NH}_2\text{SO}_3\text{H}$   
84 molecule can act as both hydrogen donors and acceptors to interact with atmospheric species.  
85 Previous studies have demonstrated that SFA has a potential role in new particle formation (NPF),  
86 as it not only clusters efficiently with itself and SA (Lovejoy and Hanson, 1996), but also can  
87 promote the nucleation rate of NPF initiated from SA-DMA by a factor of two in dry and severely  
88 contaminated areas with  $\text{NH}_3$  (Li et al., 2018). Due to the concentration of SA in the atmosphere has  
89 decreased significantly with the scenario of  $\text{SO}_2$  emission control measures, MSA-driven NPF has



90 attracted growing attention (Dawson et al., 2012; Nishino et al., 2014; Chen and Finlayson-Pitts,  
91 2017; Chen et al., 2020; Shen et al., 2020). Initially, the binary nucleation of MSA with inorganic  
92 ammonia and organic amines in the atmosphere has been reported, where MA exhibits the strongest  
93 enhancing capability (Chen et al., 2016; Chen and Finlayson-Pitts, 2017; Shen et al., 2019; Hu et  
94 al., 2023). Subsequently, some reported results suggested that the triadic MSA-MA-driven NPF can  
95 exhibit greater nucleation rates compared to the binary of MSA-driven (Zhang et al., 2022; Hu et  
96 al., 2023). For example, both formic acid (Zhang et al., 2022) and trifluoroacetic acid (Hu et al.,  
97 2023) exhibit an excellent catalytic influence on MSA-MA-driven NPF. However, the SFA  
98 involved in MSA-MA-driven NPF has not been investigated, which is worth important to  
99 investigate whether SFA can exhibit a similar enhancing effect in MSA-MA as observed in SA-  
100 DMA.

101 Herein, this work studied the catalytic effect of SFA on HNSO<sub>2</sub> hydrolysis and MSA-MA  
102 nucleation particle formation. Specifically, quantum chemical calculations were used firstly to  
103 assess the atmospheric processes of the gaseous hydrolysis of HNSO<sub>2</sub> with CH<sub>3</sub>SO<sub>3</sub>H. Then, the  
104 gaseous and interfacial mechanisms differences of the HNSO<sub>2</sub> hydrolysis with MSA were  
105 investigated applying the Born-Oppenheimer Molecular Dynamic (BOMD) simulation method.  
106 Finally, the atmospheric implications and mechanism of SFA in the MSA-MA-dominated NPF  
107 process have been evaluated through density functional theory and the Atmospheric Clusters  
108 Dynamic Code (ACDC) models to evaluate the potential effect of SFA on nucleation and NPF. This  
109 work will not only deepen our understanding of the source of SFA, but also reveal significant  
110 implications for new particle formation and aerosol particle growth in MSA polluted areas.

## 111 **2 Methodology**

### 112 **2.1 Quantum Chemical Calculations**

113 The gaseous hydrolysis of HNSO<sub>2</sub> with CH<sub>3</sub>SO<sub>3</sub>H was comprehensively studied through  
114 quantum chemistry simulations. Optimization of all the species were carried out by using the method  
115 of M06-2X with 6-311++G(2df,2pd) basis set (Zhao and Truhlar, 2008; Elm et al., 2012; Bork et al.,  
116 2014). Vibrational frequencies were subsequently computed at the M06-2X/6-311++G(2df,2pd)  
117 level to ensure the reality of all stationary point's frequencies and the presence of only one imaginary  
118 frequency in transition states. Also, at the same level, internal reaction coordinate (IRC) analyses



119 were conducted to verify the connection from the transition states to the corresponding products (or  
120 reactants). All calculations regarding for geometries and frequency were conducted with the aid of  
121 the Gaussian 09 (Frisch, 2009) program. Furthermore, to enhance the precision of the computed  
122 energy values, single point energies were performed at the CCSD(T)-F12/cc-pVDZ-F12 (Kendall  
123 et al., 1992; Adler et al., 2007) level utilizing the ORCA (Neese, 2012) program, based on the  
124 optimized geometries mentioned above.

## 125 **2.2 Rate coefficients calculations**

126 The rate coefficients for the hydrolysis of HNSO<sub>2</sub> with CH<sub>3</sub>SO<sub>3</sub>H were calculated through a  
127 two-step process. Initially, the high-pressure-limit (HPL) rate coefficients were computed applying  
128 VRC-VTST methods within the Polyrate package (Chuang et al., 1999). Subsequently, on the basis  
129 of the HPL rate coefficients, the rate coefficients for the hydrolysis of HNSO<sub>2</sub> with CH<sub>3</sub>SO<sub>3</sub>H were  
130 calculated within the temperature range of 212.6-320.0 K and pressures applying the Master  
131 Equation Solver for Multi-Energy Well Reactions (MESMER) program (Glowacki et al., 2012). The  
132 rate coefficients for the barrierless steps transitioning between reactants and pre-reactive complexes  
133 were assessed applying the Inverse Laplace Transform (ILT) method within MESMER calculations,  
134 while the step transitioning between pre-reactive complexes and post-reactive complexes via  
135 transition states were evaluated using the RRKM theory (Mai et al., 2018) in combination with the  
136 asymmetric Eckart model. The details of the rate coefficient for the hydrolysis of HNSO<sub>2</sub> without  
137 and with  $X$  ( $X = \text{H}_2\text{O}$  and  $\text{CH}_3\text{SO}_3\text{H}$ ) were given in Part 1, Table 1 and Table S4.

## 138 **2.3 BOMD Simulations**

139 BOMD simulations were conducted applying DFT implemented in CP2K program  
140 (Vandevondele et al., 2005; Hutter et al., 2014). The exchange and correlation interactions were  
141 addressed using the Becke-Lee-Yang-Parr (BLYP) functional (Becke, 1988; Lee et al., 1988),  
142 while Grimme's dispersion was applied to address weak dispersion interaction (Grimme et al.,  
143 2010). The Goedecker-Teter-Hutter (GTH) conservation pseudopotential (Goedecker et al.,  
144 1996; Hartwigsen et al., 1998) combine with Gaussian DZVP basis set (Vandevondele and  
145 Hutter, 2007) and an auxiliary plane wave basis set were used to represent core and valence  
146 electrons. Energy cutoffs (Zhong et al., 2017; Zhong et al., 2018; Zhong et al., 2019) of 280 Ry  
147 for the plane wave basis set and 40 Ry for the Gaussian basis set were applied. The gaseous  
148 reactions were simulated in the NVT ensemble at 300 K, with  $15 \times 15 \times 15 \text{ \AA}^3$  supercells and the



149 time step of 1 fs. To simulate the water microdroplet, the system containing 191  
150 (Zhong et al., 2017) was utilized in  $35 \times 35 \times 35 \text{ \AA}^3$  supercells. This setup included HNSO<sub>2</sub> and  
151 CH<sub>3</sub>SO<sub>3</sub>H along with the water drop. Prior to the interfacial simulation, a 10 ps relaxation period  
152 in the BOMD simulation was used to equilibrate the water microdroplet system with 191  
153 molecules.

#### 154 2.4 ACDC kinetics simulation

155 The ACDC model was utilized to simulate the (MSA)<sub>x</sub>(MA)<sub>y</sub>(SFA)<sub>z</sub> ( $0 \leq y \leq x + z \leq 3$ )  
156 cluster formation rates and explore the potential mechanisms. This simulation encompasses a  
157 variety of temperatures and monomer concentrations to capture the dynamics under different  
158 environmental conditions. Thermodynamic parameters, obtained from quantum chemical  
159 calculations executed at the M06-2X/6-311++G(2df,2pd) level, were used as inputs for the  
160 ACDC model. The temporal progression of cluster concentrations was determined by  
161 numerically integrating the birth-death equation, leveraging MATLAB's ode15s solver for  
162 enhanced accuracy.

$$163 \quad \frac{dc_i}{dt} = \frac{1}{2} \sum_{j < i} \beta_{j,(i-j)} c_j c_{(i-j)} + \sum_j \gamma_{(i+j) \rightarrow i} c_{i+j} - \sum_j \beta_{i,j} c_i c_j - \frac{1}{2} \sum_{j < i} \gamma_{i \rightarrow j} c_i + Q_i - S_i \quad (2)$$

164 Here,  $c_i$  represents the concentration of a specific cluster, labelled as  $i$ ; the term  $\beta_{i,j}$  was used to  
165 denote the collision coefficient, which was a measure of the frequency at which clusters  $i$  and  $j$   
166 collide with each other in a given environment or system; the coefficient  $\gamma_{(i+j) \rightarrow i}$  was defined  
167 as the evaporation rate constant that describes the process of a larger cluster, consisting of  
168 combined elements  $i$  and  $j$ , breaking down into the individual smaller clusters  $i$  and  $j$ ; and  $Q_i$   
169 encompasses all other source terms contributing to the formation of cluster  $i$ .  $S_i$  signifies  
170 alternative sink terms for cluster  $i$  that may remove it from the system.

### 171 3. Results and discussions

#### 172 3.1 The hydrolysis of HNSO<sub>2</sub> with CH<sub>3</sub>SO<sub>3</sub>H in the gas phase

173 Given the low chance of three molecules of HNSO<sub>2</sub>, H<sub>2</sub>O and CH<sub>3</sub>SO<sub>3</sub>H colliding  
174 simultaneously under atmospheric conditions, the hydrolysis of HNSO<sub>2</sub> with CH<sub>3</sub>SO<sub>3</sub>H (Channel  
175 MSA) was likely a sequential bimolecular process. As the concentration of water molecule ( $10^{18}$   
176 molecules·cm<sup>-3</sup>) in the atmosphere is much higher than those of HNSO<sub>2</sub> and CH<sub>3</sub>SO<sub>3</sub>H ( $10^5$ - $10^9$



177 molecules·cm<sup>-3</sup>), the reaction pathway of HNSO<sub>2</sub>···CH<sub>3</sub>SO<sub>3</sub>H + H<sub>2</sub>O is hard to occur in actual  
178 atmospheric conditions. So, Channel MSA proceeds through the initial formation of dimers  
179 (HNSO<sub>2</sub>···H<sub>2</sub>O and CH<sub>3</sub>SO<sub>3</sub>H···H<sub>2</sub>O) via collisions between HNSO<sub>2</sub> (or CH<sub>3</sub>SO<sub>3</sub>H) and H<sub>2</sub>O.  
180 Subsequently, the generated dimer interacts with the third reactant, either CH<sub>3</sub>SO<sub>3</sub>H or HNSO<sub>2</sub>. As  
181 seen in Fig. 1, the calculated Gibbs free energy of CH<sub>3</sub>SO<sub>3</sub>H···H<sub>2</sub>O complex was -0.9 kcal·mol<sup>-1</sup>,  
182 which was 4.5 kcal·mol<sup>-1</sup> lower than that of HNSO<sub>2</sub>···H<sub>2</sub>O. Consequently, it was predicted the  
183 primary route for the hydrolysis reaction of HNSO<sub>2</sub> with CH<sub>3</sub>SO<sub>3</sub>H takes place via the HNSO<sub>2</sub> +  
184 CH<sub>3</sub>SO<sub>3</sub>H···H<sub>2</sub>O reaction.

185 Starting from the HNSO<sub>2</sub> + CH<sub>3</sub>SO<sub>3</sub>H···H<sub>2</sub>O reactants, the Channel MSA was initiated through  
186 the intermediate complex designated as IM\_MSA1. From a geometric perspective, IM\_MSA1  
187 complex exhibits a cage-like configuration by a van der Waals force (S1···O1, 2.00 Å) and the  
188 involvement of three hydrogen bonds of H2···O4 (1.53 Å), H4···N1 (1.60 Å) and H5···O3 (2.07 Å).  
189 The Gibbs free energy of IM\_MSA1 complex relative to HNSO<sub>2</sub> + CH<sub>3</sub>SO<sub>3</sub>H···H<sub>2</sub>O reactants was  
190 1.7 kcal·mol<sup>-1</sup>. Subsequently, as presented in Fig. 1, Channel MSA progresses through transition  
191 state TS\_MSA1 to yield complex IMF\_MSA1. At TS\_MSA1, the CH<sub>3</sub>SO<sub>3</sub>H moiety facilitates two  
192 hydrogen atom transfer, with TS\_MSA1 lying only 0.8 kcal·mol<sup>-1</sup> above complex IM\_MSA1.  
193 Complex IMF\_MSA1 exhibits a cage-like structure with a Gibbs free energy was 23.4 kcal·mol<sup>-1</sup>  
194 lower than that of IM\_MSA1, revealing thermodynamic favorability of HNSO<sub>2</sub> hydrolysis with  
195 CH<sub>3</sub>SO<sub>3</sub>H. To evaluate the relative catalytic impact of CH<sub>3</sub>SO<sub>3</sub>H and H<sub>2</sub>O, Fig. S4 illustrates the  
196 profiles of Gibbs free energy for the hydrolysis of HNSO<sub>2</sub> and the corresponding reaction assisted  
197 by H<sub>2</sub>O. Compared to complex HNSO<sub>2</sub>···(H<sub>2</sub>O)<sub>2</sub>, the Gibbs stabilization energy of IM\_MSA1  
198 increased by 5.6 kcal·mol<sup>-1</sup>, potentially shortening the S1···O1 bond distance by 0.21 Å.  
199 Considering the Gibbs free energy barrier and rate coefficients, CH<sub>3</sub>SO<sub>3</sub>H demonstrates a greater  
200 catalytic role compared to H<sub>2</sub>O in lowering the energy barrier for the hydrolysis of HNSO<sub>2</sub>. In  
201 particular, CH<sub>3</sub>SO<sub>3</sub>H facilitates hydrogen atom to extraction from H<sub>2</sub>O, further reducing the reaction  
202 energy barriers to 7.7 kcal·mol<sup>-1</sup>. Meanwhile, the calculated rate coefficients for HNSO<sub>2</sub> hydrolysis  
203 with CH<sub>3</sub>SO<sub>3</sub>H was 3.08 × 10<sup>-11</sup>-3.50 × 10<sup>-11</sup> cm<sup>3</sup>·molecule<sup>-1</sup>·s<sup>-1</sup> within 212.6-320.0 K, exceeding  
204 corresponding values for reactions involving H<sub>2</sub>O by 2 orders of magnitude. Besides, the Gibbs free  
205 energy of IMF\_MSA1 was 2.0 kcal·mol<sup>-1</sup> lower than that of the product complex IMF\_WM1  
206 (NH<sub>2</sub>SO<sub>3</sub>H···H<sub>2</sub>O), suggesting NH<sub>2</sub>SO<sub>3</sub>H has a higher affinity for CH<sub>3</sub>SO<sub>3</sub>H compared to H<sub>2</sub>O.



207 Besides, CH<sub>3</sub>SO<sub>3</sub>H-assisted HNSO<sub>2</sub> hydrolysis is reduced by 4.9 kcal·mol<sup>-1</sup> in energy barrier than  
208 the NH<sub>3</sub>-assisted ammonolysis of SO<sub>3</sub> with their rate constants close each other ( $4.35 \times 10^{-10}$   
209 cm<sup>3</sup>·molecule<sup>-1</sup>·s<sup>-1</sup>) (Li et al., 2018). As the absence of the concentration of HNSO<sub>2</sub>, the  
210 competitiveness of these two reactions cannot be further confirmed.

211 To evaluate the comparative catalytic ability of  $X$  ( $X = \text{H}_2\text{O}$  and CH<sub>3</sub>SO<sub>3</sub>H) in the atmosphere,  
212 the effective rate coefficients ( $k'$ ) for  $X$ -assisted HNSO<sub>2</sub> hydrolysis were calculated in Table 1.  
213 Notably,  $k'$  serves as a metric for gauging the comparative catalytic ability of a series of gaseous  
214 catalysts in atmospheric reactions (Sarkar et al., 2017; Zhang et al., 2020; Zhang et al., 2019; Buszek  
215 et al., 2012; Gonzalez et al., 2011; Parandaman et al., 2018; Anglada et al., 2013). When  $X$  was  
216 present, the calculated  $k'$  was given by Eq. (3).

$$217 \quad k'_X = k_X \times K_{\text{eq}}(X \cdots \text{H}_2\text{O}) \times [X] \quad (3)$$

218 In Eq. (3),  $k_X$  was the rate coefficient for  $X$ -assisted HNSO<sub>2</sub> hydrolysis (Table 1), while  $K_{\text{eq}}(X \cdots \text{H}_2\text{O})$   
219 denotes the equilibrium coefficients of  $X \cdots \text{H}_2\text{O}$  (Table S2).  $[X]$  represents the available  
220 concentrations of H<sub>2</sub>O (Anglada et al., 2013) and CH<sub>3</sub>SO<sub>3</sub>H (Shen et al., 2020). As indicated in  
221 Table 1, at experimental concentrations ( $[\text{H}_2\text{O}] = 5.16 \times 10^{16}$ - $2.35 \times 10^{18}$  molecules·cm<sup>-3</sup>) within  
222 280.0-320.0 K (at 0 km), the computed  $k'_{\text{WM}}$  ranged from  $5.99 \times 10^{-18}$ - $7.79 \times 10^{-17}$  cm<sup>3</sup>·molecule<sup>-1</sup>·s<sup>-1</sup>.  
223 This range exceeded  $k'_{\text{MSA}}$  ( $4.60 \times 10^{-21}$ - $4.81 \times 10^{-20}$  cm<sup>3</sup>·molecule<sup>-1</sup>·s<sup>-1</sup>) by 2-4 orders of  
224 magnitude, highlighting pronounced impact of H<sub>2</sub>O compared to CH<sub>3</sub>SO<sub>3</sub>H at 0 km in enhancing  
225 the rate of HNSO<sub>2</sub> hydrolysis. However, with the significant decrease in atmospheric water  
226 molecules with increasing altitude, the calculated  $k'_{\text{MSA}}$  ranged from  $1.96 \times 10^{-19}$ ·s<sup>-1</sup>- $1.30 \times 10^{-17}$ ·cm<sup>3</sup>·molecule<sup>-1</sup>·s<sup>-1</sup>,  
227 surpassing  $k'_{\text{WM}}$  ( $9.85 \times 10^{-27}$ - $6.51 \times 10^{-22}$ ·cm<sup>3</sup>·molecule<sup>-1</sup>·s<sup>-1</sup>) by 3-10 orders  
228 of magnitude. This illustrates that CH<sub>3</sub>SO<sub>3</sub>H has a significantly greater catalytic ability than H<sub>2</sub>O  
229 in accelerating the rate of HNSO<sub>2</sub> hydrolysis within 0-10 km. So, HNSO<sub>2</sub> hydrolysis with CH<sub>3</sub>SO<sub>3</sub>H  
230 may represent a potential formation pathway for NH<sub>2</sub>SO<sub>3</sub>H across an altitude scope of 5-15 km.

### 231 3.2 Reactions at the air-water interface

232 The interfacial mechanism of CH<sub>3</sub>SO<sub>3</sub>H-assisted HNSO<sub>2</sub> hydrolysis at the air-water  
233 interface has not been thoroughly investigated. Interestingly, our simulations show that HNSO<sub>2</sub> and  
234 CH<sub>3</sub>SO<sub>3</sub>H molecules spend approximately 49.1% and 12.1% of the time, respectively, at the air-  
235 water interface during the 150 ns simulation (Fig. S1 and Fig. S6). This reveals that the presence of  
236 HNSO<sub>2</sub> and CH<sub>3</sub>SO<sub>3</sub>H at the air-water interface should not be disregarded. Therefore, BOMD





237 simulations were performed to clarify the interfacial mechanism of  $\text{CH}_3\text{SO}_3\text{H}$ -assisted  $\text{HNSO}_2$   
238 hydrolysis at the air-water interface. Comparable to the reactions of  $\text{SO}_3$  at the air-water interface  
239 with acidic molecules (Cheng et al., 2023; Zhong et al., 2019a), the hydrolysis of  $\text{HNSO}_2$  with  
240  $\text{CH}_3\text{SO}_3\text{H}$  at the air-water interface may occur through three pathways: (i) the adsorbed  $\text{CH}_3\text{SO}_3\text{H}$   
241 interacts with  $\text{HNSO}_2$  at the air-water interface; (ii) the adsorbed  $\text{HNSO}_2$  interacts with  $\text{CH}_3\text{SO}_3\text{H}$   
242 at the air-water interface; and (iii) the  $\text{HNSO}_2 \cdots \text{CH}_3\text{SO}_3\text{H}$  complex reacts at the air-water interface.  
243 Nevertheless, because of the high reactivity of  $\text{CH}_3\text{SO}_3\text{H}$  at the air-water interface, the lifetime  
244 of  $\text{CH}_3\text{SO}_3\text{H}$  was minimal (seen in Fig. S9) on the water droplet, which was around a small number  
245 of picoseconds leading to the rapid formation of  $\text{CH}_3\text{SO}_3\text{H}^-$  ion. Meanwhile, although  $\text{HNSO}_2$   
246 remains stable at the air-water interface (seen in Fig. S8) and does not dissociate within 10 ps, the  
247 hydrated form of  $\text{HNSO}_2$  illustrated in Fig. S8 was not conducive to  $\text{HNSO}_2$  hydrolysis at the air-  
248 water interface. So, model (iii) was primarily considered for  $\text{HNSO}_2$  hydrolysis with  $\text{CH}_3\text{SO}_3\text{H}$  at  
249 the air-water interface. It was worth noting that  $\text{HNSO}_2 \cdots \text{CH}_3\text{SO}_3\text{H}$  complex can persist at the air-  
250 water interface for approximately 34.2% of the 150 ns simulation time (see in Fig. S7). For model  
251 (iii), two types of reactions were found at the air-water interface: (a) the  $\text{NH}_2\text{SO}_3^-$  and  $\text{H}_3\text{O}^+$  ions  
252 formation mechanism, and (b) the proton exchange mechanism.

253  **$\text{NH}_2\text{SO}_3^-$  and  $\text{H}_3\text{O}^+$  ions forming mechanism.** Fig. 2(a), Fig. S10 and Movie 1 illustrates the  
254 formation mechanism of  $\text{NH}_2\text{SO}_3^-$  and  $\text{H}_3\text{O}^+$  ions through the chain structure. At 4.57 ps, a chain  
255 hydrolyzed transition state was observed, accompanied by two protons transfer events. Specially,  
256 an H2 atom transferred from the OH moiety of  $\text{CH}_3\text{SO}_3\text{H}$  molecule to the terminal N atom of  
257  $\text{HNSO}_2$  molecule, resulting in the breaking of the O3-H2 bond (with the length of 1.49 Å) and  
258 forming the H2-N bond (with the length of 1.14 Å). Concurrently, an interfacial water molecule  
259 decomposes, leading to the elongation of the O1-H1 bond to over 1.00 Å, with the S1 atom of  
260  $\text{HNSO}_2$  obtaining the OH moiety of the interfacial water molecule ( $d_{\text{S1-O1}} = 1.60$  Å). By 4.61 ps,  
261 The N-H2 and S1-O1 bonds both shortened to 0.99 Å and 1.01 Å, revealing the formation of the  
262  $\text{NH}_2\text{SO}_3\text{H}$  molecule. However, due to its strong acidity, the  $\text{NH}_2\text{SO}_3\text{H}$  molecule could only persist  
263 on the water droplet surface for a ps time-scale. As a result, at 7.43 ps, the proton of  $\text{NH}_2\text{SO}_3\text{H}$   
264 transferred to another interfacial water molecule, completing the deprotonation of  $\text{NH}_2\text{SO}_3\text{H}$ . The  
265 loop structure mechanism (Fig. 2(b), Fig. S11 and Movie 2) was similar with the chain structure  
266 mechanism. However, in this case, the proton of  $\text{NH}_2\text{SO}_3\text{H}$  transferred to  $\text{CH}_3\text{SO}_3^-$  rather than to an



267 interfacial water molecule.

268 **Proton exchange mechanism.** As depicted in Fig. 3, the proton exchange mechanism  
269 illustrates the deprotonation of  $\text{CH}_3\text{SO}_3\text{H}$  concurrent with  $\text{HNSO}_2$  hydration at the air-water  
270 interface. As shown in Fig. 3(a), Fig. S12 and Movie 3,  $\text{CH}_3\text{SO}_3\text{H}$ -mediated hydration  $\text{HNSO}_2$  with  
271 a single water molecule was observed. Initially, the  $\text{HNSO}_2 \cdots \text{CH}_3\text{SO}_3\text{H}$  complex quickly associates  
272 with an interfacial water molecule, and forms a loop structure complex that accelerates the rate of  
273 proton transfer. By 4.38 ps, an eight-membered loop structure complex,  $\text{HNSO}_2 \cdots \text{H}_2\text{O} \cdots \text{CH}_3\text{SO}_3\text{H}$ ,  
274 emerges, characterized by two hydrogen bonds ( $d_{(\text{H}_2-\text{N})} = 1.82 \text{ \AA}$  and  $d_{(\text{H}_1-\text{O}_2)} = 1.92 \text{ \AA}$ ) and a van  
275 der Waals forces ( $d_{(\text{S}_1-\text{O}_1)} = 2.35 \text{ \AA}$ ). Thereafter, at 4.77 ps, a transition state-like configuration was  
276 identified where the water molecule within the loop complex dissociated, elongating the O1-H1  
277 bond to over  $1.00 \text{ \AA}$ , and the S atom of  $\text{HNSO}_2$  attaches to the OH group of the interfacial water  
278 molecule. Concurrently, the  $\text{CH}_3\text{SO}_3^-$  ion receives the proton from the separated interfacial water  
279 molecule. The entire reaction for  $\text{CH}_3\text{SO}_3\text{H}$ -mediated hydration  $\text{HNSO}_2$  with one water molecule  
280 was completed at 4.80 ps, resulting in the formation of  $\text{NH}_2\text{SO}_3\text{H}$  and  $\text{CH}_3\text{SO}_3\text{H}$  molecules.  
281  $\text{CH}_3\text{SO}_3\text{H}$ -mediated hydration of  $\text{HNSO}_2$  with two water molecules (Fig. 3(b), Fig. S13 and Movie  
282 4) at the air-water interface was similar with mechanism identified with one water molecule.  
283 However, the inclusion of two water molecules enlarges the loop, significantly reducing the stress  
284 on the loop structures. Consistent with the prediction in Fig. 4, the loop structures preferred to  
285 include two water molecules rather than one water molecule. This observation agrees well with the  
286 reported hydration of Criegee intermediate at the air-water interface (Zhu et al., 2016; Kumar et al.,  
287 2018; Liu et al., 2021; Zhang et al., 2023a). Additionally,  $\text{CH}_3\text{SO}_3\text{H}$ -mediated hydration of  $\text{HNSO}_2$   
288 with three water molecules (Fig. S14 and Movie 5) has been observed in the proton exchange  
289 mechanism. However, its probability of occurrence was smaller due to the relatively larger entropy  
290 effect. It was noteworthy that the  $\text{NH}_2\text{SO}_3\text{H}$  and  $\text{CH}_3\text{SO}_3\text{H}$  molecules formed in the proton exchange  
291 mechanism were not stable at the air-water interface, which can further interact with an interfacial  
292 water molecule to form the corresponding ions of  $\text{NH}_2\text{SO}_3^-$  and  $\text{CH}_3\text{SO}_3^-$ .

293 At the air-water interface, a sum of 50 BOMD trajectories, each lasting 10 ps, were conducted  
294 to investigate  $\text{HNSO}_2$  hydrolysis with  $\text{CH}_3\text{SO}_3\text{H}$ . Two distinct mechanisms were observed: the  
295 formation of  $\text{NH}_2\text{SO}_3^-$  and  $\text{H}_3\text{O}^+$  ions formation (shown in blue and yellow in Fig. 4) and the proton  
296 exchange mechanism (represented by orange, purple and green in Fig. 4). In the mechanism



297 involving the formation of  $\text{NH}_2\text{SO}_3^-$  and  $\text{H}_3\text{O}^+$  ions, approximately 22% (Fig. 2(a), Fig. 4, Fig. S10  
298 and Movie 1) of the reactions took place via a chain structure, while the majority (~18%) (Fig. 2(b),  
299 Fig. 4, Fig. S11 and Movie 2) proceeded through a loop structure mechanism. This discrepancy can  
300 be attributed to the uncertainty regarding the direction of proton transfer from  $\text{NH}_2\text{SO}_3\text{H}$ . Since the  
301 number of water molecules near the water microdroplet far exceeded that of  $\text{CH}_3\text{SO}_3^-$ , protons were  
302 predominantly transferred to interface water molecules, making the loop structure mechanism  
303 weaker than the chain structure mechanism. Approximately 60% of the reactions were observed to  
304 be due to the proton exchange mechanism in BOMD simulations. Through water-mediated  
305 mechanisms, these reactions resulted in  $\text{NH}_2\text{SO}_3\text{H}$  formation. Similarly to gas-phase reactions, loop  
306 structures were observed in these reactions. Approximately 10% of the reactions formed a loop  
307 structure involving one water molecule (Fig. 3(a), Fig. 4, Fig. S12 and Movie 3), while the most  
308 common loop structure involved two water molecules (about 42%) (Fig. 3(b), Fig. 4, Fig. S13 and  
309 Movie 4). Smaller loops were found to experience more stress than loop structures with two water  
310 molecules. In cases of loop structures with three water molecules (about 8%) (Fig. 4, Fig. S14 and  
311 Movie 5), the entropy effect was deemed to be more significant than the strain effect and likely  
312 played a dominant role. The two water molecules contained in the loop structure not only acted as  
313 a reactant but also facilitated proton transfer as a bridge.

### 314 **3.3 New Particle Formation from the atmospheric products**

#### 315 **3.3.1. The influence of SFA on the stability of atmospheric MSA-MA-based** 316 **clusters**

317 Electrostatic Potential (ESP) mapping on the molecular van der Waals (vdW) surface was  
318 employed to analyze the interactions between SFA and other key nucleation precursors like MSA  
319 and MA. As shown in Fig. 5, sites with more negative ESP often attract more positive ESP sites,  
320 namely hydrogen bonds in the studied system. Specifically, the hydrogen atoms of the  $-\text{SO}_3\text{H}$  and  
321  $\text{NH}_2$  groups (site 4 and 5) in SFA, possessing more positive ESP values, have the potential to attract  
322 groups with negative ESP values, such as the oxygen atom within the  $-\text{SO}_3\text{H}$  group of MSA (site 6)  
323 and the nitrogen atom of MA (site 1), thus forming hydrogen bonds as proton donors. Additionally,  
324 the sulfur atom of the  $-\text{SO}_3\text{H}$  functional group (site 7) in SFA, with a negative ESP of -30.75, acts  
325 as proton acceptor, facilitating direct binding with MSA and MA molecules via the hydrogen bonds.



326 Therefore, the introduction of SFA was believed to enhance the stability of MSA-MA clusters by  
327 promoting the formation of more hydrogen bonds and facilitating proton transfers.

### 328 **3.3.2. The cluster formation rates in the SFA-MSA-MA system**

329 Simulations were conducted to determine the cluster formation rates ( $J$ ) for the MSA-MA-SFA  
330 system, varying parameters such as temperature and the concentrations of the precursors were  
331 involved. To assess the promotional impact of SFA on  $J$  under varying atmospheric conditions, the  
332 enhancement factor ( $R$ ) was computed as the ratio of  $J_{MSA-MA-SFA}$  to  $J_{MSA-MA}$ . As depicted in Fig. 6  
333 (a), the  $J$  of MSA-MA-SFA system exhibits a negative correlation with temperature, attributed to  
334 the decrease in  $\Delta G$  value and evaporation rates of clusters at lower temperatures. Conversely, a  
335 positive correlation of  $R$  with temperature was observed (Fig. 6(b)), indicating that SFA's  
336 enhancement of nucleation was more pronounced in regions with relatively higher temperatures.  
337 Furthermore, both  $J$  and  $R$  show an increase as the [SFA] increases, suggesting a positive correlation  
338 of  $J$  and  $R$  with [SFA]. In short, in regions with high [SFA], such as the Yangtze River Delta of  
339 China, Bangladesh, and the east coast of India, SFA was expected to significantly boost the  $J$  of  
340 MSA-MA based nucleation. It is noted that in Fig. 6(b), due to the competitive relationship between  
341 MSA and SFA, at low concentrations of SFA, the binding capacity of MSA with MA is stronger  
342 than that of SFA with MA, resulting in only a small amount of SFA participating in cluster formation.  
343 However, as the concentration of SFA increases, the number of  $(MSA)_x \cdot (MA)_y \cdot (SFA)_z$  (where  $y \leq$   
344  $x + z \leq 3$ ) ternary clusters increases, leading to the formation of more hydrogen bonds and a  
345 significant increase in  $R_{SFA}$ . Additionally, Fig. 7 illustrates the  $J$  and  $R$  of MSA-MA-SFA clusters  
346 under different [MSA] and [MA]. On one hand, larger values of [MSA] and [MA] correspond to  
347 higher  $J$ , as the increased concentration of nucleation precursors leads to a rise in the number of  
348 MSA-MA-SFA clusters. On the other hand, increasing [MSA] and [MA] result in a decrease in the  
349  $R$  attributed to the effect of SFA on nucleation. This was because as [MSA] and [MA] increases,  
350 the prevalence of pure MSA-MA clusters rise during the clustering process, consequently reducing  
351 the impact of SFA.

### 352 **3.3.3. The growth paths of cluster under different atmospheric conditions**

353 In Fig. 8 (a), two main types of cluster formation routes were found: (i) the pure MSA-MA  
354 pathway and (ii) the MSA-MA-SFA pathways at 278.15 K in the studied system. In the pure MSA-  
355 MA pathway, cluster growth primarily occurs through the collisional addition of MSA or MA  
356 monomers. Conversely, in the SFA-involved pathways, SFA can directly participate in the



357 formation of stable larger clusters subsequently, such as  $(\text{MSA})_2 \cdot (\text{MA})_2 \cdot \text{SFA}$  and  
358  $(\text{MSA})_2 \cdot (\text{MA})_2 \cdot (\text{SFA})_2$  clusters, and then subsequently grow out. The involvement of SFA in the  
359 cluster formation pathway was significantly influenced by atmospheric conditions. Firstly, as the  
360 temperature rises from 238.15 K to 278.15 K, the contribution of the SFA-involved cluster  
361 formation pathways rises from 68% to 90% (Fig. 8 (b)), implying that the pathway involving SFA  
362 becomes increasingly important at lower altitudes or in warmer conditions. Secondly, the  
363 contribution of the pathway with SFA exhibits a negative correlation with [SA] (Fig. 8 (c)),  
364 attributed to the competitive relationship between SFA and MSA. Thirdly, the contribution of the  
365 SFA-involved cluster formation pathway was positively associated with the concentration of [SFA]  
366 (Fig. 8 (d)). At  $[\text{SFA}] = 10^4 \text{ molecules} \cdot \text{cm}^{-3}$ , the pathway involving SFA was not prominent, and the  
367 pure MSA-MA pathway dominates. However, as [SFA] rises from  $10^4$  to  $10^8 \text{ molecules} \cdot \text{cm}^{-3}$ , the  
368 contribution of the SFA-involved pathway increased from 7% to 98% at 278.15 K. Therefore, the  
369 pathway involving SFA appears to dominate near SFA release sources in warm temperatures or at  
370 lower altitudes.

### 371 **3.4 Interfacial implications of products on aerosol particle growth**

372 As the discussion above, the formation of  $\text{SFA}^- \cdots \text{H}_3\text{O}^+$  and  $\text{MSA}^- \cdots \text{H}_3\text{O}^+$  ions pairs can occur  
373 within a few picoseconds at the air-water interface. The atmospheric affinity of  $\text{MSA}^-$ ,  $\text{SFA}^-$  and  
374  $\text{H}_3\text{O}^+$  for gaseous precursors was further probed by evaluating the free energies of interaction. It  
375 was worth noting that compounds such as MSA, MA,  $\text{HNO}_3$  (NA), and  $(\text{COOH})_2$  (OA) were  
376 identified as candidate species for consideration (Wang et al., 2024; Kulmala et al., 2004). As  
377 presented in Table 2, the computed binding energies demonstrate that the interactions of  $\text{SFA}^-$   
378  $\cdots \text{MSA}$ ,  $\text{SFA}^- \cdots \text{NA}$ ,  $\text{SFA}^- \cdots \text{OA}$ ,  $\text{H}_3\text{O}^+ \cdots \text{MA}$ ,  $\text{MSA}^- \cdots \text{MSA}$ ,  $\text{MSA}^- \cdots \text{OA}$ , and  $\text{MSA}^- \cdots \text{NA}$  were  
379 stronger than those of  $\text{MSA}^- \cdots \text{MA}$  (one of the primary precursors for atmospheric aerosols), with  
380 their Gibbs free energies increased by 14.3-50.9  $\text{kcal} \cdot \text{mol}^{-1}$ . The findings indicate that the presence  
381 of  $\text{SFA}^-$ ,  $\text{MSA}^-$ , and  $\text{H}_3\text{O}^+$  at the interface facilitates the capture of potential gaseous species onto  
382 the surface of water microdroplet.

383 Furthermore, we investigated the possibility of  $\text{SFA}^-$  contributing to the enlargement of  
384 particles within the MSA-MA cluster, taking into account the geometric configuration and the free  
385 energy of formation for the  $(\text{MSA})_1 \cdot (\text{MA})_1 \cdot (\text{SFA}^-)_1$  clusters aggregating. Compared with other  
386 clusters, such as  $(\text{MSA})_1 \cdot (\text{MA})_1 \cdot (\text{X})_1$  (where  $\text{X} = \text{HCOOH}$ ,  $\text{CH}_3\text{COOH}$ ,  $\text{CHOCOOH}$ ,  $\text{OA}$ ,  
387  $\text{CH}_3\text{COCO OH}$ ,  $\text{HOOCCH}_2\text{COOH}$ ,  $\text{HOOC}(\text{CH})_2\text{COOH}$ ,  $\text{HOOC}(\text{CH}_2)_2\text{COOH}$ ,



388 HOOC(CH<sub>2</sub>)<sub>3</sub>COOH, C<sub>6</sub>H<sub>5</sub>(COOH) and C<sub>10</sub>H<sub>16</sub>O<sub>3</sub>) clusters (Zhang et al, 2022), the quantity of  
389 hydrogen bonds within the (MSA)<sub>1</sub>·(MA)<sub>1</sub>·(SFA<sup>-</sup>)<sub>1</sub> cluster has increased, and the loop of complex  
390 was expanded. It has been demonstrated that SFA<sup>-</sup> has the greatest capacity to stabilize MSA-MA  
391 clusters and facilitate MSA-MA nucleation in these clusters. This was attributed to its acidic nature  
392 and structural characteristics, which include a greater number of intermolecular hydrogen bond  
393 binding sites. Therefore, relative to (MSA)<sub>1</sub>·(MA)<sub>1</sub>·(X)<sub>1</sub> cluster (Table 2), the Gibbs formation free  
394 energy  $\Delta G$  of the (MSA)<sub>1</sub>·(MA)<sub>1</sub>·(SFA<sup>-</sup>)<sub>1</sub> cluster was lower, indicating that the NH<sub>2</sub>SO<sub>3</sub><sup>-</sup> ion  
395 exhibits a more potent nucleation capacity at the air-water interface compared to the X species in  
396 the gas phase. Consequently, our forecast was that the presence of NH<sub>2</sub>SO<sub>3</sub><sup>-</sup> at the air-water interface  
397 will foster enhanced particle growth.

#### 398 4. Summary and Conclusions

399 In this study, quantum chemical calculations, BOMD simulations and ACDC kinetic model  
400 were utilized to characterize the gaseous and interfacial hydrolysis of HNSO<sub>2</sub> with CH<sub>3</sub>SO<sub>3</sub>H, and  
401 to examine the influence exerted by NH<sub>2</sub>SO<sub>3</sub>H on MSA-MA-based clusters.

402 In the gaseous reaction, the activation energy for the hydrolysis of HNSO<sub>2</sub> catalyzed by  
403 CH<sub>3</sub>SO<sub>3</sub>H was only 0.8 kcal·mol<sup>-1</sup>, significantly lower by 7.7 kcal·mol<sup>-1</sup> than the energy barrier of  
404 H<sub>2</sub>O-assisted HNSO<sub>2</sub> hydrolysis. The effective rate coefficients reveal that the NH<sub>2</sub>SO<sub>3</sub>H formation  
405 from CH<sub>3</sub>SO<sub>3</sub>H-catalyzed hydrolysis of HNSO<sub>2</sub> can be competitive with that catalyzed by H<sub>2</sub>O  
406 within an altitude of 5-15 km. Moreover, kinetic simulations utilizing the ACDC have disclosed that  
407 SFA has an unexpectedly positive impact on the NPF process, markedly enhancing the assembly of  
408 MSA-MA-based cluster. Notably, the “participant” mechanism of SFA for cluster formation has  
409 been identified by tracing the growth paths of the system in agriculture-developed and coastal  
410 industrial areas, especially significant in the Yangtze River Delta of China, Bangladesh, and the east  
411 coast of India.

412 At the air-water interface, the NH<sub>2</sub>SO<sub>3</sub><sup>-</sup> and H<sub>3</sub>O<sup>+</sup> ions forming mechanism (~40%) and the  
413 proton exchange mechanism (~60%) were observed in the hydrolysis of HNSO<sub>2</sub> with CH<sub>3</sub>SO<sub>3</sub>H,  
414 which can take place in a few picoseconds. Notably, the formed NH<sub>2</sub>SO<sub>3</sub><sup>-</sup>, CH<sub>3</sub>SO<sub>3</sub><sup>-</sup>, and H<sub>3</sub>O<sup>+</sup> ions  
415 at the air-water interface possess the ability to attract potential precursor molecules like CH<sub>3</sub>SO<sub>3</sub>H,  
416 CH<sub>3</sub>NH<sub>2</sub>, and HNO<sub>3</sub>. This attraction facilitates the transition of gaseous molecules onto the surface



417 of water microdroplet. Moreover, the assessment of the potential of  $X$  in the formation of the ternary  
418  $\text{CH}_3\text{SO}_3\text{H}-\text{CH}_3\text{NH}_2-X$  cluster revealed that  $\text{NH}_2\text{SO}_3^-$  exhibits the greatest propensity to stabilize  
419  $\text{CH}_3\text{SO}_3\text{H}-\text{CH}_3\text{NH}_2$  clusters and to foster nucleation of  $\text{CH}_3\text{SO}_3\text{H}-\text{CH}_3\text{NH}_2$  in the context of  $X$ .

420 Overall, this work not only elucidates a novel mechanism underlying the hydrolysis of  $\text{HNSO}_2$   
421 with  $\text{CH}_3\text{SO}_3\text{H}$ , but also highlight the potential contribution of SFA on aerosol particle growth and  
422 new particle formation.

### 423 **Acknowledgments**

424 This work was supported by the National Natural Science Foundation of China (No: 22203052;  
425 22073059); the Key Cultivation Project of Shaanxi University of Technology (No: SLG2101); the  
426 Education Department of Shaanxi Provincial Government (No. 23JC023).

### 427 **Declaration of competing interest**

428 The authors declare that they have no known competing financial interests or personal  
429 relationships that could have appeared to influence the work reported in this paper.



## 430 Reference

- 431 Adler, T. B., Knizia, G., and Werner, H. J.: A simple and efficient CCSD(T)-F12 approximation, *J. Chem.*  
432 *Phys.*, 127, 22, 2007.
- 433 Anglada, J. M., Hoffman, G. J., Slipchenko, L. V. M., Costa, M., Ruiz-Lopez, M. F., and Francisco, J. S.:  
434 Atmospheric significance of water clusters and ozone-water complexes, *J. Phys. Chem. A*, 117, 10381-  
435 10396, 2013.
- 436 Becke, A. D.: Density-functional exchange-energy approximation with correct asymptotic behavior,  
437 *Phys. Rev. A*, 38, 3098-3100, 1988.
- 438 Berresheim, H., Elste, T., Tremmel, H. G., Allen, A. G., Hansson, H. C., Rosman, K., Dal Maso, M.,  
439 Mäkelä, J. M., Kulmala, M., and O'Dowd, C. D.: Gas-aerosol relationships of H<sub>2</sub>SO<sub>4</sub>, MSA, and OH:  
440 Observations in the coastal marine boundary layer at Mace Head, Ireland, *J. Geophys. Res. Atmos.*, 107,  
441 PAR 5-1-PAR 5-12, 2002.
- 442 Bork, N., Elm, J., Olenius, T., and Vehkamäki, H.: Methane sulfonic acid-enhanced formation of  
443 molecular clusters of sulfuric acid and dimethyl amine, *Atmos. Chem. Phys.*, 14, 12023-12030, 2014.
- 444 Bork, N., Du, L., Reiman, H., Kurten, T., and Kjaergaard, H. G.: Benchmarking ab initio binding energies  
445 of hydrogen-bonded molecular clusters based on FTIR spectroscopy, *J. Phys. Chem. A*, 118, 5316-5322,  
446 2014.
- 447 Buszek, R. J., Torrent-Sucarrat, M., Anglada, J. M., and Francisco, J. S.: Effects of a single water  
448 molecule on the OH + H<sub>2</sub>O<sub>2</sub> reaction, *J. Phys. Chem. A*, 116, 5821-5829, 2012.
- 449 Chen, D., Li, D., Wang, C., Luo, Y., Liu, F., and Wang, W.: Atmospheric implications of hydration on the  
450 formation of methanesulfonic acid and methylamine clusters: A theoretical study, *Chemosphere.*, 244,  
451 125538-125547, <https://doi.org/10.1016/j.chemosphere.2019.125538>, 2020.
- 452 Chen, H. and Finlayson-Pitts, B. J.: New particle formation from methanesulfonic acid and  
453 amines/ammonia as a function of temperature, *Environ. Sci. Technol.*, 51, 243-252,  
454 <https://doi.org/10.1021/acs.est.6b04173>, 2017.
- 455 Chen, H., Varner, M. E., Gerber, R. B., Finlayson-Pitts, B. J., Reactions of methanesulfonic acid with  
456 amines and ammonia as a source of new particles in air. *J. Phys. Chem. B* 2016, 120, 1526-1536.
- 457 Cheng, Y., Ding, C., Wang, H., Zhang, T., Wang, R., Muthiah, B., Xu, H., Zhang, Q., and Jiang, M.:  
458 Significant influence of water molecules on the SO<sub>3</sub> + HCl reaction in the gas phase and at the air-water  
459 interface, *Phys. Chem. Chem. Phys.*, 25, 28885-28894, 2023.
- 460 Chuang, Y., Corchado, J., Fast, P., Villa, J., Coitino, E., Hu, W., Liu, Y., Lynch, G., Nguyen, K., and  
461 Jackels, C.: Polyrate-version 8.2, University of Minnesota, Minneapolis, 1999.
- 462 Dawson, M. L., Varner, M. E., Perraud, V., Ezell, M. J., Gerber, R. B., and Finlayson-Pitts, B. J.:  
463 Simplified mechanism for new particle formation from methanesulfonic acid, amines, and water via  
464 experiments and ab initio calculations, *Proc. Natl. Acad. Sci. USA.*, 109, 18719-18724, 2012.
- 465 Dawson, M. L., Varner, M. E., Perraud, V. M., Ezell, M. J., Wilson, J. M., Zelenyuk, A., Gerber, R. B.,  
466 and Finlayson-Pitts, B. J.: Amine-amine exchange in aminium-methanesulfonate aerosols, *J. Phys. Chem.*  
467 *C.*, 118(50):29431-29440, 2014.
- 468 Deng, G., Wu, Z., Li, D., Linguerra, R., Francisco, J. S., and Zeng, X. J. J. o. t. A. C. S.: Simplest N-  
469 Sulfonylamine HNSO<sub>2</sub>, *J. Am. Chem. Soc.*, 140, 138, 11509-11512, 2016.
- 470 Elm, J.: Clusteromics II: methanesulfonic acid-base cluster formation, *ACS omega.*, 6, 17035-17044,  
471 <https://doi.org/10.1021/acsomega.1c02115>, 2021.
- 472 Elm, J., Bilde, M., and Mikkelsen, K. V.: Assessment of density functional theory in predicting structures





- 473 and free energies of reaction of atmospheric prenucleation clusters, *J. Chem. Theory Comput.*, 8, 2071-  
474 2077, 2012.
- 475 Freeling, F., Scheurer, M., Sandholzer, A., Armbruster, D., Nödler, K., Schulz, M., Ternes, T. A., and  
476 Wick, A.: Under the radar – Exceptionally high environmental concentrations of the high production  
477 volume chemical sulfamic acid in the urban water cycle, *Water Research.*, 175, 115706,  
478 <https://doi.org/10.1016/j.watres.2020.115706>, 2020.
- 479 Frisch, M. J., Trucks, G. W., Schlegel, H. B., Scuseria, G. E., Robb, M. A., Cheeseman, J. R., Scalmani,  
480 G., Barone, V., Mennucci, B., Petersson, G. A., Nakatsuji, H., Caricato, M., Li, X., Hratchian, H. P.,  
481 Izmaylov, A. F., Bloino, J., Zheng, G., Sonnenberg, J. L., Hada, M., Ehara, M., Toyota, K., Fukuda, R.,  
482 Hasegawa, J., Ishida, M., Nakajima, T., Honda, Y., Kitao, O., Nakai, H., Vreven, T., Montgomery, J. A.  
483 Jr., Peralta, J. E., Ogliaro, F., Bearpark, M., Heyd, J. J., Brothers, E., Kudin, K. N., Staroverov, V. N.,  
484 Kobayashi, R., Normand, J., Raghavachari, K., Rendell, A., Burant, J. C., Iyengar, S. S., Tomasi, J., Cossi,  
485 M., Rega, N., Millam, J. M., Klene, M., Knox, J. E., Cross, J. B., Bakken, V., Adamo, C., Jaramillo, J.,  
486 Gomperts, R., Stratmann, R. E., Yazyev, O., Austin, A. J., Cammi, R., Pomelli, C., Ochterski, J. W.,  
487 Martin, R. L., Morokuma, K., Zakrzewski, V. G., Voth, G. A., Salvador, P., Dannenberg, J. J., Dapprich,  
488 S., Daniels, A. D., Farkas, Ö., Foresman, J. B., Ortiz, J. V., Cioslowski, J., and Fox, D. J: Gaussian09  
489 Revision D. 01, Gaussian Inc. Wallingford CT, Gaussian Inc. Wallingford CT, See also: URL: <http://www.gaussian.com>, 2009.
- 491 Glowacki, D. R., Liang, C.-H., Morley, C., Pilling, M. J., and Robertson, S. H.: MESMER: an open-  
492 source master equation solver for multi-energy well reactions, *J. Phys. Chem. A*, 116, 9545-9560, 2012.
- 493 Goedecker, S., Teter, M., and Hutter, J.: Separable dual-space Gaussian pseudopotentials, *Phys. Rev. B.*,  
494 54, 1703, 1996.
- 495 Gonzalez, J., Anglada, J. M., Buszek, R. J., and Francisco, J. S.: Impact of water on the OH + HOCl  
496 reaction, *J. Am. Chem. Soc.*, 133, 3345-3353, 2011.
- 497 Grimme, S., Antony, J., Ehrlich, S., and Krieg, H.: A consistent and accurate ab initio parametrization of  
498 density functional dispersion correction (DFT-D) for the 94 elements H-Pu, *J. Chem. Phys.*, 132, 154104,  
499 2010.
- 500 Hartwigsen, C., Goedecker, S., and Hutter, J.: Relativistic separable dual-space Gaussian  
501 pseudopotentials from H to Rn, *Phys. Rev. B.*, 58, 3641-3662, 1998.
- 502 Hirota, K., Mäkelä, J., and Tokunaga, O.: Reactions of sulfur dioxide with ammonia: Dependence on  
503 oxygen and nitric oxide, *Ind. Eng. Chem. Res.*, 35, 3362-3368, 1996.
- 504 Hu, Y., Chen, S., Ye, S., Wei, S., Chu, B., Wang, R., Li, H., and Zhang, T.: The role of trifluoroacetic acid  
505 in new particle formation from methanesulfonic acid-methylamine, *Atmos. Environ.*, 311, 120001,  
506 <https://doi.org/10.1016/j.atmosenv.2023>.
- 507 Hutter, J., Iannuzzi, M., Schiffmann, F., and VandeVondele, J.: cp2k: atomistic simulations of condensed  
508 matter systems, *WIRES COMPUT MOL SCI.*, 4, 15-25, 2014.
- 509 Kendall, R. A., T. H. D., and Harrison, R. J.: Electron affinities of the first-row atoms revisited.  
510 Systematic basis sets and wave functions, *J. Chem. Phys.*, 96, 6796-6806,  
511 <https://doi.org/10.1063/1.462569>, 1992.
- 512 Kim, T. O., Ishida, T., Adachi, M., Okuyama, K., and Seinfeld, J. H.: Nanometer-sized particle formation  
513 from NH<sub>3</sub>/SO<sub>2</sub>/H<sub>2</sub>O/air mixtures by ionizing irradiation, *Aerosol Sci. Tech.*, 29, 111-125, 1998.
- 514 Koeberg-Telder, A., Lambrechts, H. J., and Cerfontain, H.: Solutes in sulfuric acid. Part VIII. Protonation  
515 of phenol, 4-fluorophenol and the 2-and 4-sulfonates of anisole and phenol in concentrated aqueous  
516 sulfuric acid; determination of pKa values by means of <sup>13</sup>C NMR, *Recl. Trav. Chim. Pays-Bas*, 102,



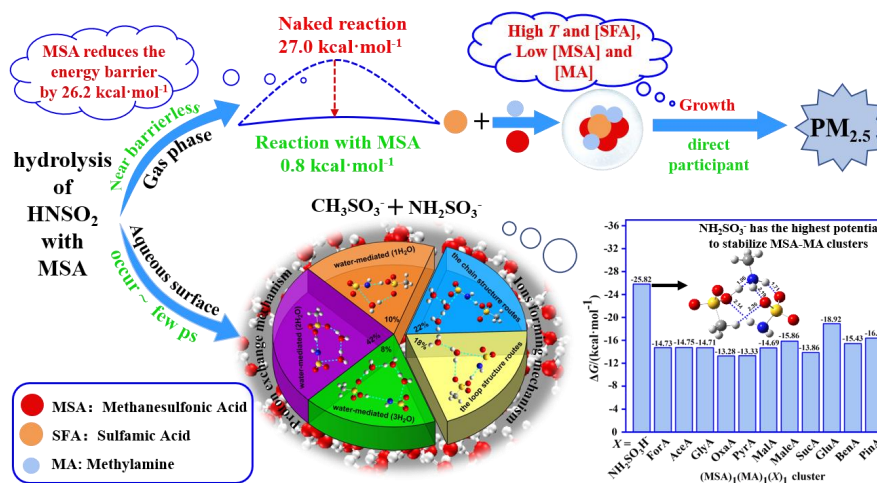
- 517 293-298, 1983.
- 518 Kolthoff, I. M. and Chantooni, M. K.: Dissociation constant,  $K_a$ , and stability constant,  $K(HA_2^-)$ , of the  
519 1:1 homoconjugate of sulfuric and nitric acids in acetonitrile at 298.1 K. *J. Chem. Eng. Data*, 44, 124-  
520 129, 1999.
- 521 Kulmala, M., Vehkamäki, H., Petäjä, T., Dal Maso, M., Lauri, A., Kerminen, V. M., Birmili, W., and  
522 McMurry, P. H.: Formation and growth rates of ultrafine atmospheric particles: a review of observations,  
523 *J. Aerosol Sci.*, 35, 143-176, <https://doi.org/10.1016/j.jaerosci.2003.10.003>, 2004.
- 524 Kumar, M., Li, H., Zhang, X., Zeng, X. C., and Francisco, J. S.: Nitric acid-amine chemistry in the gas  
525 phase and at the air-water interface, *J. Am. Chem. Soc.*, 140, 6456-6466, 2018.
- 526 Kuttippurath, J., Singh, A., Dash, S., Mallick, N., Clerbaux, C., Van Damme, M., Clarisse, L., Coheur,  
527 P.-F., Raj, S., and Abbhishek, K.: Record high levels of atmospheric ammonia over India: Spatial and  
528 temporal analyses, *Sci. Total Environ.*, 740, 139986, 2020.
- 529 Larson, L. J. and Tao, F.-M.: Interactions and reactions of sulfur trioxide, water, and ammonia: An ab  
530 initio and density functional theory study, *J. Phys. Chem. A*, 105, 4344-4350, 2001.
- 531 Lee, C., Yang, W., and Parr, R. G.: Development of the colle-Salvetti correlation-energy formula into a  
532 functional of the electron density, *PHYS REV B*, 37, 785, 1988.
- 533 Li, H., Zhong, J., Vehkamäki, H., Kurtén, T., Wang, W., Ge, M., Zhang, S., Li, Z., Zhang, X., Francisco,  
534 J. S., and Zeng, X. C.: Self-Catalytic reaction of  $SO_3$  and  $NH_3$  to produce sulfamic acid and its implication  
535 to atmospheric particle formation, *J. Am. Chem. Soc.*, 140, 11020-11028,  
536 <https://doi.org/10.1021/jacs.8b04928>, 2018.
- 537 Liu, J., Liu, Y., Yang, J., Zeng, X. C., and He, X.: Directional proton transfer in the reaction of the simplest  
538 criegee intermediate with water involving the formation of transient  $H_3O^+$ , *J. Phys. Chem. Lett.*, 12,  
539 3379-3386, <https://doi.org/10.1021/acs.jpcclett.1c00448>, 2021.
- 540 Lovejoy, E. R. and Hanson, D. R.: Kinetics and products of the reaction  $SO_3 + NH_3 + N_2$ , *J. Phys. Chem.*,  
541 100, 4459-4465, <https://doi.org/10.1021/jp952404x>, 1996.
- 542 Ma, X., Zhao, X., Huang, Z., Wang, J., Lv, G., Xu, F., Zhang, Q., and Wang, W.: Determination of  
543 reactions between Criegee intermediates and methanesulfonic acid at the gas-liquid interface, *Sci. Total*  
544 *Environ.*, 707, 135804, 2020.
- 545 Mai, T. V. T., Duong, M. V., Nguyen, H. T., and Huynh, L. K.: Ab initio kinetics of the  $HOSO_2 + ^3O_2 \rightarrow$   
546  $SO_3 + HO_2$  reaction, *Phys. Chem. Chem. Phys.*, 20, 6677-6687, 2018.
- 547 Manonmani, G., Sandhiya, L., and Senthilkumar, K. J. I. J. O. Q. C.: Hydrolysis of  $HNSO_2$ : A potential  
548 route for atmospheric production of  $H_2SO_4$  and  $NH_3$ , *Int. J. Quantum Chem.*, 120, e26182, 2020.
- 549 Neese, F.: The ORCA program system, *WIREs Comput. Mol. Sci.*, 2, 73-78, 2012.
- 550 Parandaman, A., Perez, J. E., and Sinha, A.: Atmospheric decomposition of trifluoromethanol catalyzed  
551 by formic acid, *J. Phys. Chem. A*, 122, 9553-9562, 2018.
- 552 Prue, J. and Read, A.: Acidity constant of formic acid, *Trans. Faraday Soc.*, 62, 1271-1274, 1966.
- 553 Pszona, M., Haupa, K., Bil, A., Mierzwicki, K., Szewczuk, Z., and Mielke, Z.: Clustering of sulfamic  
554 acid: ESI MS and theoretical study, *J. Mass Spectrom.*, 50, 127-135, 2015.
- 555 Rennebaum, T., van Gerven, D., Sebastian, S. S., and Wickleder, M. S.: Hydrazine sulfonic acid,  $NH_3NH$   
556  $(SO_3)$ , the bigger sibling of sulfamic acid, *CHEM-EUR J*, 30, e202302526, 2024.
- 557 Sarkar, S., Mallick, S., Kumar, P., and Bandyopadhyay, B.: Isomerization of methoxy radical in the  
558 troposphere: Competition between acidic, neutral and basic catalysts, *Phys. Chem. Chem. Phys.*, 19,  
559 27848-27858, 2017.
- 560 Shang, D., Tang, L., Fang, X., Wang, L., Yang, S., Wu, Z., Chen, S., Li, X., Zeng, L., Guo, S., and Hu,



- 561 M.: Variations in source contributions of particle number concentration under long-term emission control  
562 in winter of urban Beijing, *Environ. Pollut.*, 304, 119072, <https://doi.org/10.1016/j.envpol.2022.119072>,  
563 2022.
- 564 Shen, J., Elm, J., Xie, H.-B., Chen, J., Niu, J., and Vehkamäki, H.: Structural effects of amines in  
565 enhancing methanesulfonic acid-driven new particle formation, *Environ. Sci. Technol.*, 54, 13498-13508,  
566 2020.
- 567 Shen, J., Xie, H.-B., Elm, J., Ma, F., Chen, J., and Vehkamäki, H.: Methanesulfonic acid-driven new  
568 particle formation enhanced by monoethanolamine: A computational study, *Environ. Sci. Technol.*, 53,  
569 14387-14397, 2019.
- 570 Chen, H.; Varner, M. E.; Gerber, R. B.; Finlayson-Pitts, B. J.: Reactions of methanesulfonic acid with  
571 amines and ammonia as a source of new particles in air, *J. Phys. Chem. B*, 120, 1526-1536, 2016.
- 572 Shi, Z., Ford, J., and Castleman Jr, A.: Cluster reactions of sulfur trioxide and ammonia, *Chemical*  
573 *physics letters*, 220, 274-280, 1994.
- 574 Tang, Y. S., Flechard, C. R., Dämmgen, U., Vidic, S., Djuricic, V., Mitosinkova, M., Uggerud, H. T., Sanz,  
575 M. J., Simmons, I., and Dragosits, U.: Pan-European rural monitoring network shows dominance of NH<sub>3</sub>  
576 gas and NH<sub>4</sub>NO<sub>3</sub> aerosol in inorganic atmospheric pollution load, *Atmos. Chem. Phys.*, 21, 875-914,  
577 2021.
- 578 Van Stempvoort, D., Spoelstra, J., Brown, S., Robertson, W., Post, R., and Smyth, S.: Sulfamate in  
579 environmental waters, *Sci. Total Environ.*, 695, 133734, 2019.
- 580 VandeVondele, J. and Hutter, J.: Gaussian basis sets for accurate calculations on molecular systems in  
581 gas and condensed phases, *J. Chem. Phys.*, 127, 114105, 2007.
- 582 VandeVondele, J., Krack, M., Mohamed, F., Parrinello, M., Chassaing, T., and Hutter, J.: Quickstep: Fast  
583 and accurate density functional calculations using a mixed Gaussian and plane waves approach, *Comput.*  
584 *Phys. Commun.*, 167, 103-128, 2005.
- 585 Wang, R., Carnevale, V., Klein, M. L., and Borguet, E.: First-Principles calculation of water p<sub>k</sub> a using  
586 the newly developed scan functional, *J. Phys. Chem. Lett.*, 11, 54-59, 2019.
- 587 Wang, R., Cheng, Y., Chen, S., Li, R., Hu, Y., Guo, X., Zhang, T., Song, F., and Li, H.: Reaction of SO<sub>3</sub>  
588 with H<sub>2</sub>SO<sub>4</sub> and its implications for aerosol particle formation in the gas phase and at the air-water  
589 interface, *Atmos. Chem. Phys.*, 24, 4029-4046, 2024.
- 590 Wang, S., Nan, J., Shi, C., Fu, Q., Gao, S., Wang, D., Cui, H., Saiz-Lopez, A., and Zhou, B.: Atmospheric  
591 ammonia and its impacts on regional air quality over the megacity of Shanghai, China, *Sci. Rep.*, 5, 15842,  
592 2015.
- 593 Warner, J. X., Wei, Z., Strow, L. L., Dickerson, R. R., Nowak, J. B., and Physics: The global tropospheric  
594 ammonia distribution as seen in the 13-year AIRS measurement record, *Atmos. Chem. Phys.*, 16, 5467-  
595 5479, 2016.
- 596 Xue, J., Shao, X., Li, J., Li, J., Trabelsi, T., Francisco, J. S., and Zeng, X.: Observation of the Water-  
597 HNSO<sub>2</sub> complex, *J. Am. Chem. Soc.*, 146, 5455-5460, 2024.
- 598 Yu, X., Shen, L., Hou, X., Yuan, L., Pan, Y., An, J., and Yan, S.: High-resolution anthropogenic ammonia  
599 emission inventory for the Yangtze River Delta, China, *CHEMOSPHERE*, 251, 126342, 2020.
- 600 Zhang, R., Khalizov, A., Wang, L., Hu, M., and Xu, W.: Nucleation and growth of nanoparticles in the  
601 atmosphere, *Chem. Rev.*, 112, 1957-2011, 2012.
- 602 Zhang, R., Shen, J., Xie, H. B., Chen, J., and Elm, J.: The role of organic acids in new particle formation  
603 from methanesulfonic acid and methylamine, *Atmos. Chem. Phys.*, 22, 2639-2650,  
604 <https://doi.org/10.5194/acp-22-2639-2022>, 2022.



- 605 Zhang, T., Wen, M., Cao, X., Zhang, Y., Zeng, Z., Guo, X., Zhao, C., Lily, M., and Wang, R.: The  
606 hydrolysis of NO<sub>2</sub> dimer in small clusters of sulfuric acid: A potential source of nitrous acid in  
607 troposphere, *Atmos. Environ.*, 243, 117876, <https://doi.org/10.1016/j.atmosenv.2020.117876>, 2020.
- 608 Zhang, T., Wen, M., Ding, C., Zhang, Y., Ma, X., Wang, Z., Lily, M., Liu, J., and Wang, R.: Multiple  
609 evaluations of atmospheric behavior between Criegee intermediates and HCHO: Gas-phase and gas-  
610 liquid interface reaction, *J. Environ. Sci.*, 127, 308-319, <https://doi.org/10.1016/j.jes.2022.06.004>, 2023.
- 611 Zhang, T., Wen, M., Zhang, Y., Lan, X., Long, B., Wang, R., Yu, X., Zhao, C., and Wang, W.: Atmospheric  
612 chemistry of the self-reaction of HO<sub>2</sub> radicals: stepwise mechanism versus one-step process in the  
613 presence of (H<sub>2</sub>O)<sub>n</sub> (*n* = 1-3) clusters, *Phys. Chem. Chem. Phys.*, 21, 24042-24053,  
614 <https://doi.org/10.1039/C9CP03530C>, 2019.
- 615 Zhang, T., Zhang, Y., Tian, S., Zhou, M., Liu, D., Lin, L., Zhang, Q., Wang, R., and Muthiah, B.: Possible  
616 atmospheric source of NH<sub>2</sub>SO<sub>3</sub>H: the hydrolysis of HNSO<sub>2</sub> in the presence of neutral, basic, and acidic  
617 catalysts, *Phys. Chem. Chem. Phys.*, 24, 4966-4977, 2022.
- 618 Zhang, Y., Wang, Z., Wang, H., Cheng, Y., Zhang, T., Ou, T., and Wang, R.: Atmospheric chemistry of  
619 NH<sub>2</sub>SO<sub>3</sub>H in polluted areas: an unexpected isomerization of NH<sub>2</sub>SO<sub>3</sub>H in acid-polluted regions, *J. Phys.*  
620 *Chem. A*, 127, 8935-8942, 2023.
- 621 Zhao, Y. and Truhlar, D. G.: The M06 suite of density functionals for main group thermochemistry,  
622 thermochemical kinetics, noncovalent interactions, excited states, and transition elements: two new  
623 functionals and systematic testing of four M06-class functionals and 12 other functionals, *Theor. Chem.*  
624 *Acc.*, 120, 215-241, 2008.
- 625 Zhong, J., Kumar, M., Francisco, J. S., and Zeng, X. C.: Insight into chemistry on cloud/aerosol water  
626 surfaces, *Acc. Chem. Res.*, 51, 1229-1237, 2018.
- 627 Zhong, J., Kumar, M., Zhu, C. Q., Francisco, J. S., and Zeng, X. C.: Frontispiece: surprising stability of  
628 larger criegee intermediates on aqueous interfaces, *ANGEW CHEM INT EDIT*, 56, 7740-7744,  
629 <https://doi.org/10.1002/anie.201782761>, 2017.
- 630 Zhong, J., Li, H., Kumar, M., Liu, J., Liu, L., Zhang, X., Zeng, X. C., and Francisco, J. S.: Mechanistic  
631 insight into the reaction of organic acids with SO<sub>3</sub> at the air-water interface, *ANGEW CHEM INT EDIT*,  
632 131, 8351-8355, 2019.
- 633 Zhu, C., Kumar, M., Zhong, J., Li, L., Francisco, J. S., and Zeng, X. C.: New mechanistic pathways for  
634 Criegee-water chemistry at the air/water interface, *J. Am. Chem. Soc.*, 138, 11164-11169, 2016.



635

636

Graphical abstract



### Figure Captions

- 637
- 638 **Fig. 1** The potential energy profile ( $\Delta G$ ) for the hydrolysis reaction of  $\text{HNSO}_2$  with  $\text{CH}_3\text{SO}_3\text{H}$  at the  
639 CCSD(T)-F12/cc-pVDZ-F12//M06-2X/6-311++G(2df,2pd) level of theory  
640  
641
- 642 **Fig. 2** BOMD simulation trajectories and snapshots of  $\text{NH}_2\text{SO}_3^-$  and  $\text{H}_3\text{O}^+$  ions forming mechanism  
643 (chain structure (a) and loop-structure (b)) in the  $\text{HNSO}_2$  hydrolysis with  $\text{CH}_3\text{SO}_3\text{H}$  at the air-water  
644 interface  
645  
646
- 647 **Fig. 3** BOMD simulation trajectories and snapshots of proton exchange mechanism in  $\text{CH}_3\text{SO}_3\text{H}$ -  
648 mediated hydration  $\text{HNSO}_2$  with one (a) and two (b) water molecules at the air-water interface  
649  
650
- 651 **Fig. 4** Percentages of different mechanisms for the  $\text{HNSO}_2$  hydrolysis with  $\text{CH}_3\text{SO}_3\text{H}$  at the air-  
652 water interface observed in BOMD simulations  
653  
654
- 655 **Fig. 5** ESP-mapped molecular vdW surface of MA, SFA and MSA molecules at M06-2X/6-  
656 311++G(2df,2pd) level of theory. Surface local minima and maxima of ESP of the different  
657 functional groups in MA, SFA and MSA molecules are represented as blue and yellow spheres,  
658 respectively. The values of maximum and minimum are shown in kcal mol<sup>-1</sup> in the parentheses. The  
659 green, red and blue arrows refer to the tendencies to form hydrogen bonds and proton transfer events,  
660 respectively. (green = carbon, red = oxygen, blue = nitrogen, yellow = sulfur and white = hydrogen.)  
661  
662
- 663 **Fig. 6** The  $J$  (cm<sup>3</sup> s<sup>-1</sup>) (a) and  $R$  (b) versus [SFA] with [MSA] = 10<sup>6</sup> molecules cm<sup>-3</sup>, [MA] = 2.5 ×  
664 10<sup>8</sup> molecules cm<sup>-3</sup> and four different temperatures (green line: 298.15 K, blue line: 278.15 K, red  
665 line: 258.15 K, black line: 238.15 K).  
666  
667
- 668 **Fig. 7** The  $J$  (cm<sup>3</sup> s<sup>-1</sup>) (a) and  $R$  (b) as a function of [MSA] with [SFA] = 10<sup>8</sup> molecules cm<sup>-3</sup> and  
669 three different [MA] (black line: [MA] = 2.5 × 10<sup>7</sup> molecules cm<sup>-3</sup>, red line: [MA] = 2.5 × 10<sup>8</sup>  
670 molecules cm<sup>-3</sup>, blue line: [MA] = 2.5 × 10<sup>9</sup> molecules cm<sup>-3</sup>) at 278.15 K.  
671  
672
- 673 **Fig. 8** Main cluster formation mechanism of MSA-MA-SFA-based system at 278.15 K, [MSA] =  
674 10<sup>7</sup> molecules·cm<sup>-3</sup>, [MA] = 2.5 × 10<sup>8</sup> molecules·cm<sup>-3</sup>, and [SFA] = 10<sup>6</sup> molecules·cm<sup>-3</sup>. (a) The  
675 black arrows indicate the pure MSA-MA-based growth pathways. Blue arrows represent the  
676 pathways containing SFA. The influence of (b) temperature, (c) [SFA] and (d) [MSA] on the relative  
677 contribution of the pure MSA-MA-based clustering pathway and the SFA participation pathway to  
678 the system flux is analyzed. Others in (b), (c), and (d) indicate that the pathway contribution of the  
679 cluster growing out of the studied system is less than 5%

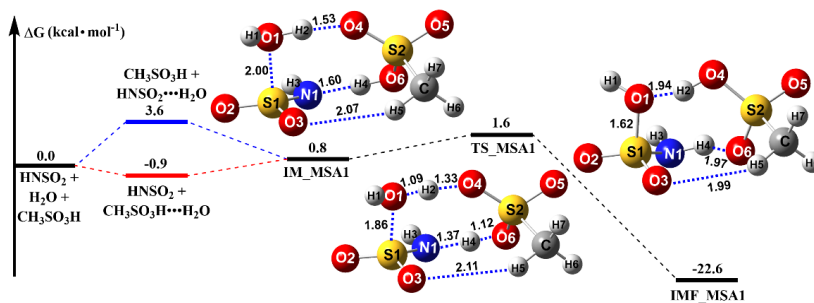
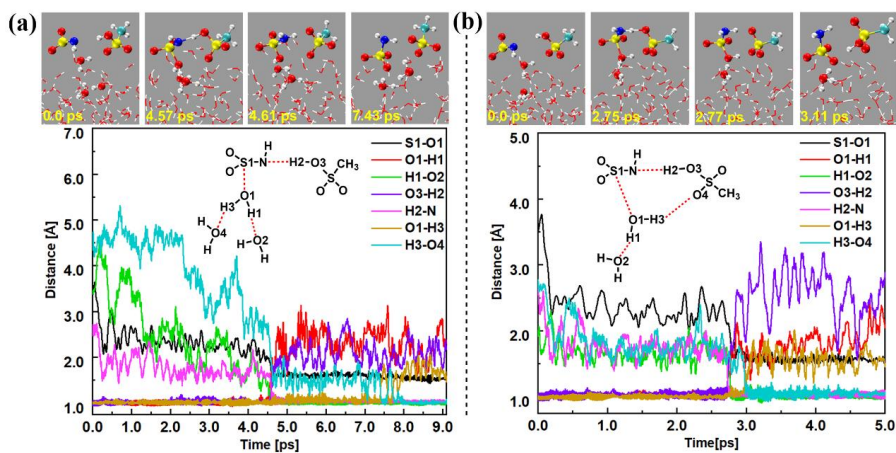


Fig. 1

680

681

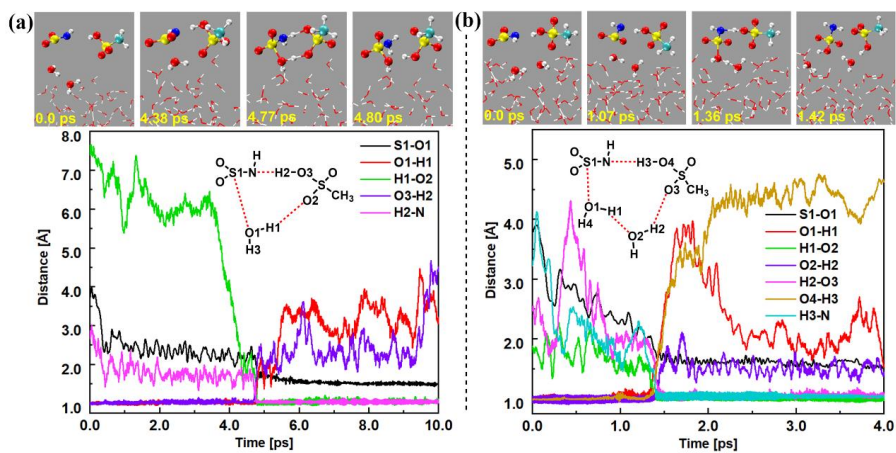


682

683

Fig. 2





684

685

686

Fig. 3

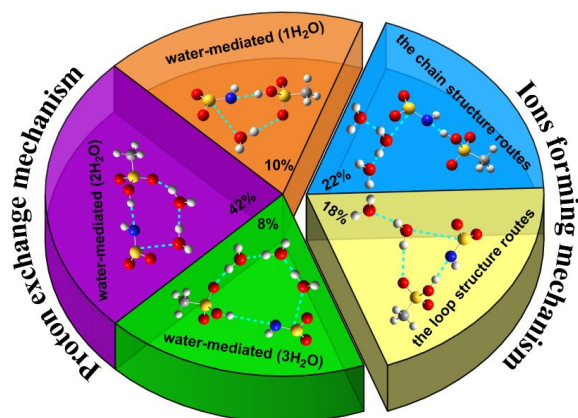
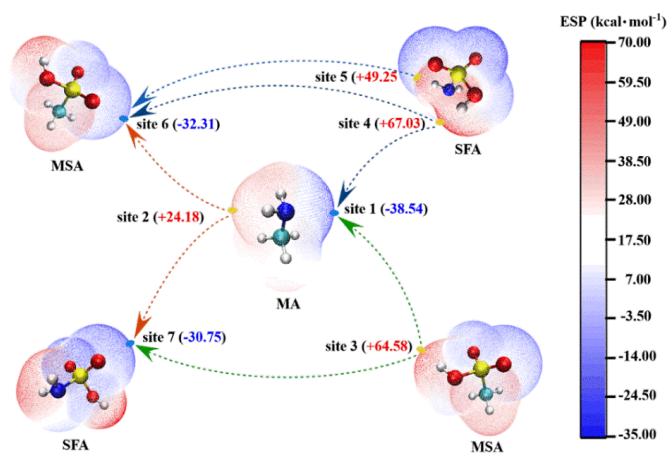


Fig. 4

687

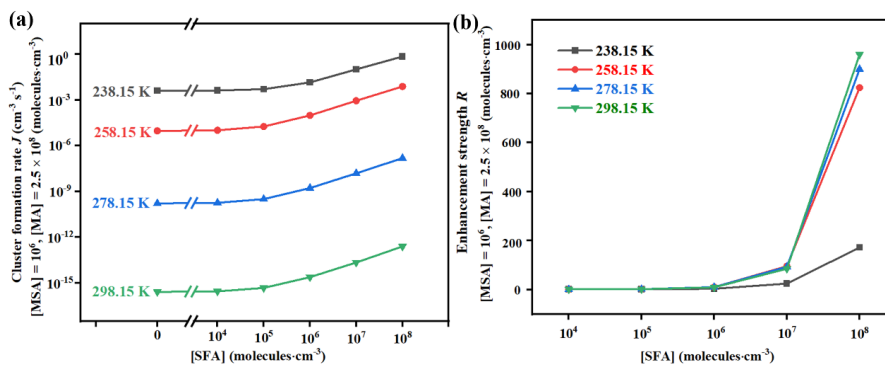
688



689

690

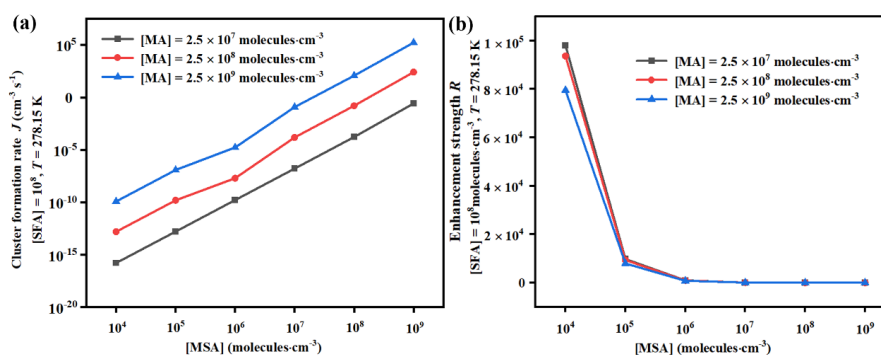
Fig. 5



691

692

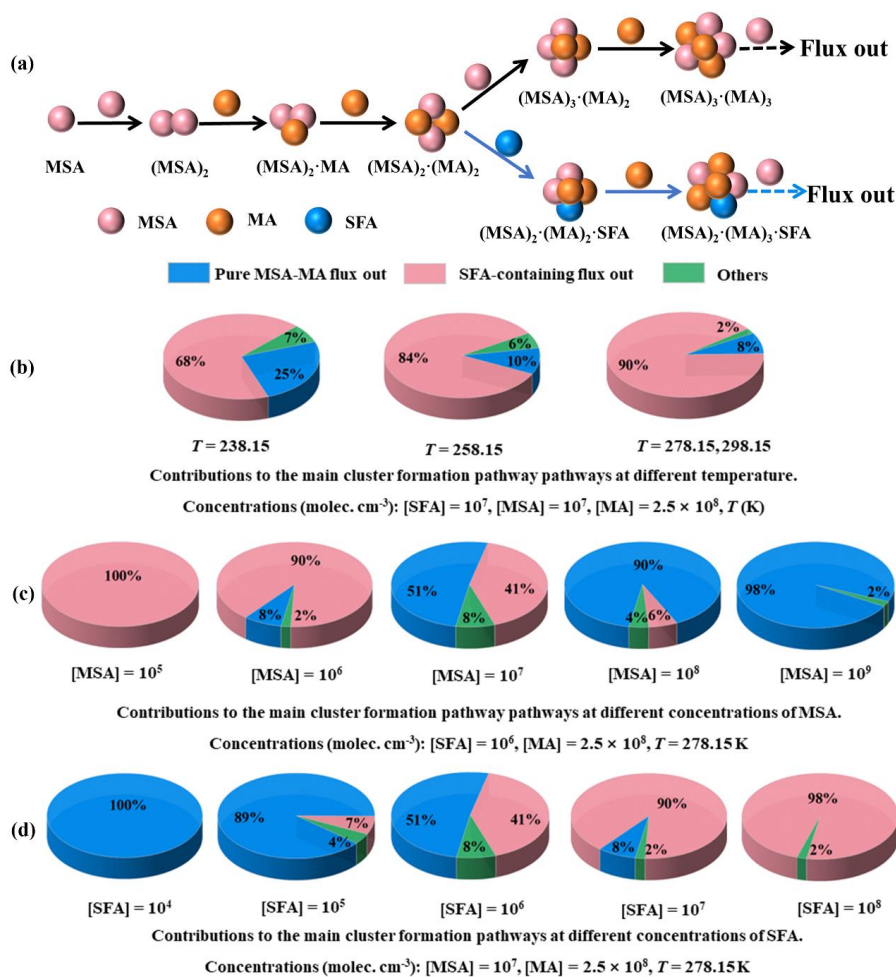
Fig. 6



693

694

Fig. 7



695

696

Fig. 8



697

**Table 1** Rate coefficients ( $k$ ,  $\text{cm}^3 \cdot \text{molecule}^{-1} \cdot \text{s}^{-1}$ ) and effective rate constants ( $k'$ ,  $\text{cm}^3 \cdot \text{molecule}^{-1} \cdot \text{s}^{-1}$ ) for the hydrolysis of  $\text{HNSO}_2$  with  $\text{H}_2\text{O}$  and  $\text{CH}_3\text{SO}_3\text{H}$  calculated by master equation within the temperature range of 213–320 K and altitude range of 0–15 km

Altitude	280	290	298	300	310	320	5 km	10 km	15 km
T/K									
$k_{\text{WM}}$	$7.64 \times 10^{-13}$	$6.45 \times 10^{-13}$	$5.63 \times 10^{-13}$	$5.44 \times 10^{-13}$	$4.59 \times 10^{-13}$	$3.88 \times 10^{-13}$	$1.09 \times 10^{-12}$	$1.72 \times 10^{-12}$	$2.22 \times 10^{-12}$
$k_{\text{MSA}}$	$3.08 \times 10^{-11}$	$2.96 \times 10^{-11}$	$2.85 \times 10^{-11}$	$2.82 \times 10^{-11}$	$2.67 \times 10^{-11}$	$2.52 \times 10^{-11}$	$3.32 \times 10^{-11}$	$3.49 \times 10^{-11}$	$3.50 \times 10^{-11}$
20%RH	$5.99 \times 10^{-18}$	$7.96 \times 10^{-18}$	$9.64 \times 10^{-18}$	$1.03 \times 10^{-17}$	$1.29 \times 10^{-17}$	$1.36 \times 10^{-17}$			
40%RH	$1.19 \times 10^{-17}$	$1.58 \times 10^{-17}$	$1.99 \times 10^{-17}$	$2.07 \times 10^{-17}$	$2.60 \times 10^{-17}$	$3.12 \times 10^{-17}$			
60%RH	$1.79 \times 10^{-17}$	$2.38 \times 10^{-17}$	$2.98 \times 10^{-17}$	$3.11 \times 10^{-17}$	$3.90 \times 10^{-17}$	$4.68 \times 10^{-17}$	$9.85 \times 10^{-27}$	$1.71 \times 10^{-22}$	$6.51 \times 10^{-22}$
80%RH	$2.39 \times 10^{-17}$	$3.17 \times 10^{-17}$	$3.97 \times 10^{-17}$	$4.14 \times 10^{-17}$	$5.21 \times 10^{-17}$	$6.24 \times 10^{-17}$			
100%RH	$2.97 \times 10^{-17}$	$3.96 \times 10^{-17}$	$4.97 \times 10^{-17}$	$5.18 \times 10^{-17}$	$6.50 \times 10^{-17}$	$7.79 \times 10^{-17}$			
$k_{\text{MSA}}$	$4.81 \times 10^{-19}$	$2.50 \times 10^{-19}$	$1.57 \times 10^{-19}$	$1.40 \times 10^{-19}$	$7.90 \times 10^{-20}$	$4.60 \times 10^{-20}$	$1.96 \times 10^{-20}$	$2.37 \times 10^{-19}$	$1.30 \times 10^{-18}$
$k_{\text{MSA}}/k_{\text{WM}}$	$1.62 \times 10^{-4}$	$6.42 \times 10^{-5}$	$3.16 \times 10^{-5}$	$2.69 \times 10^{-5}$	$1.22 \times 10^{-5}$	$5.90 \times 10^{-5}$	$3.01 \times 10^1$	$1.38 \times 10^3$	$1.32 \times 10^8$

$k_{\text{WM}}$  and  $k_{\text{MSA}}$  are respectively the rate constant for the hydrolysis of  $\text{HNSO}_2$  with  $\text{H}_2\text{O}$  and  $\text{CH}_3\text{SO}_3\text{H}$ ;  $k'_{\text{WM}}$  and  $k'_{\text{MSA}}$  are respectively the effective rate constant for the hydrolysis of  $\text{HNSO}_2$  with  $\text{H}_2\text{O}$  and  $\text{CH}_3\text{SO}_3\text{H}$ .



698 **Table 2.** Gibbs free energy ( $\Delta G$ ) for the formation of SFA $\cdots$ MSA, SFA $\cdots$ NA, SFA $\cdots$ OA,  
 699 H<sub>3</sub>O<sup>+</sup> $\cdots$ MA, MSA $\cdots$ MSA, MSA $\cdots$ OA, and MSA $\cdots$ NA, MSA $\cdots$ MA, (MSA)<sub>1</sub>(MA)<sub>1</sub>(X)<sub>1</sub> at 298  
 700 K

	SFA $\cdots$ MSA	SFA $\cdots$ HNO <sub>3</sub>	SFA $\cdots$ OA	MSA $\cdots$ MSA	MSA $\cdots$ NA
$\Delta G$	-23.8	-21.5	-25.2	-23.9	-22.6
	MSA $\cdots$ OA	MSA $\cdots$ H <sub>3</sub> O <sup>+</sup>	MA $\cdots$ H <sub>3</sub> O <sup>+</sup>	MSA $\cdots$ MA	
$\Delta G$	-25.8	-35.8	-57.9	-7.0 (-7.2) <sup>b</sup>	
	HCOOH	CH <sub>3</sub> COOH	CHOCOOH	OA	
	$\cdots$ MSA $\cdots$ MA	$\cdots$ MSA $\cdots$ MA	$\cdots$ MSA $\cdots$ MA	$\cdots$ MSA $\cdots$ MA	
$\Delta G$	-14.7 (-15.8) <sup>a</sup>	-14.8 (-14.3) <sup>a</sup>	-14.7 (-15.6) <sup>a</sup>	-13.3 (-12.7) <sup>a</sup>	
	CH <sub>3</sub> COCOOH	HOOCCH <sub>2</sub> COOH	HOOC(CH <sub>2</sub> ) <sub>2</sub> COOH	HOOC(CH <sub>2</sub> ) <sub>2</sub> COOH	
	$\cdots$ MSA $\cdots$ MA	$\cdots$ MSA $\cdots$ MA	$\cdots$ MSA $\cdots$ MA	$\cdots$ MSA $\cdots$ MA	
$\Delta G$	-13.3 (-13.0) <sup>a</sup>	-14.7 (-16.7) <sup>a</sup>	-15.9 (-15.3) <sup>a</sup>	-13.9 (-14.3) <sup>a</sup>	
	HOOC(CH <sub>2</sub> ) <sub>3</sub> COOH	C <sub>6</sub> H <sub>5</sub> (COOH)	C <sub>10</sub> H <sub>16</sub> O <sub>3</sub>	SFA $\cdots$	
	$\cdots$ MSA $\cdots$ MA	$\cdots$ MSA $\cdots$ MA	$\cdots$ MSA $\cdots$ MA	$\cdots$ MSA $\cdots$ MA	
$\Delta G$	-18.9 (-17.9) <sup>a</sup>	-15.4 (-15.3) <sup>a</sup>	-16.4 (-15.3) <sup>a</sup>	-25.8	

701 <sup>a</sup> The value was taken from reference (Zhang, R., Shen, J., Xie, H. B., Chen, J., and Elm, J.: The role of organic acids  
 702 in new particle formation from methanesulfonic acid and methylamine, Atmos. Chem. Phys., 22, 2639-2650,  
 703 10.5194/acp-22-2639-2022, 2022b.)

704 <sup>b</sup> The value was taken from reference (Zhong, J., Li, H., Kumar, M., Liu, J., Liu, L., Zhang, X., Zeng, X. C., and  
 705 Francisco, J. S.: Mechanistic Insight into the Reaction of Organic Acids with SO<sub>3</sub> at the Air–Water Interface, Angew.  
 706 Chem. Int. Ed., 131, 8439-8443, 2019.)